CrossMark

J. Fluid Mech. (2016), *vol.* 786, *pp.* 253–274. © Cambridge University Press 2015
doi:10.1017/jfm.2015.663

Complete self-preservation along the axis of a circular cylinder far wake

S. L. Tang[1,2], R. A. Antonia[2], L. Djenidi[2,†] and Y. Zhou[1]

[1]Institute for Turbulence–Noise–Vibration Interaction and Control, Shenzhen Graduate School, Harbin Institute of Technology, Shenzhen 518055, PR China

[2]School of Engineering, University of Newcastle, NSW 2308, Australia

(Received 16 June 2015; revised 25 August 2015; accepted 4 November 2015; first published online 1 December 2015)

Self-preservation (SP) analyses are applied to the mean momentum and the scale-by-scale energy budget equations in the far wake of a circular cylinder. The scale-by-scale SP analysis, which is a two-point analysis, complements the SP analysis of the mean momentum equation. Power-law variations are derived for different length scales (e.g. the Taylor microscale and the Kolmogorov length scale) and velocity scales (e.g. the root mean square and the Kolmogorov velocity scale). Further, the SP solutions for the scale-by-scale energy budget equation are exploited to develop an exact relation to estimate the mean turbulent kinetic energy dissipation rate $\bar{\epsilon}$ on the wake axis. These SP solutions and the new $\bar{\epsilon}$ relation are well supported by hot-wire data in the far wake at a Reynolds number of 2000 based on the free stream velocity and the cylinder diameter. On the far-wake axis, both the energy spectra and the structure functions exhibit an almost perfect collapse over all wavenumbers and separations, irrespective of the set of scaling variables used for normalisation. This is consistent with a complete self-preservation (i.e. SP is satisfied at all scales of motion) in the far wake.

Key words: turbulence theory, turbulent flows, wakes

1. Introduction

Using a self-preservation (SP) analysis, which assumes that the flow is governed by a single set of length and velocity scales, Townsend (1956) identified the plane wake as a possible turbulent flow with the mean flow satisfying SP. Since then, SP has been extensively used to describe the spatial evolution of one-point statistics in the far field of the plane wake. While, in theory, SP solutions are independent of the initial conditions (hereafter denoted ICs), questions were raised about the possibility of their dependence on ICs in actual turbulent flows. George (1989), who has recently reviewed the effect of ICs of SP in the more general context of shear flows (George 2012), was the first to raise the issue of IC dependence of the SP solutions, and stated that there exists a multiplicity of SP states (for a particular flow), and that each state is uniquely determined by its ICs. George (1989) departed from the classical formulation of SP by assuming that SP solutions do not depend on a

† Email address for correspondence: lyazid.djenidi@newcastle.edu.au

https://doi.org/10.1017/jfm.2015.663 Published online by Cambridge University Press

single velocity scale. Interestingly enough, he did not consider the case where the SP solutions do not depend on a single length scale. It should be stated that Townsend (1976) considered two SP velocity scales, u_o and q_o, the former for the mean velocity and the latter for Reynolds stresses and the turbulent kinetic energy. He showed that $u_o \sim q_o$ when SP is applied to both complete mean momentum and mean turbulent kinetic energy equations, where all terms are included. George (1989) applied SP to first-order approximation only, where several terms, such as that involving viscosity, are neglected. Nevertheless, there appears to be now ample evidence that suggests that the state of SP that is reached in the far wake does depend on the initial conditions (e.g. Wygnanski, Champagne & Marasli 1986; George 1989; Zhou & Antonia 1995; Antonia & Mi 1998; Zhou, Antonia & Tsang 1998).

Almost all SP analyses have been performed on single-point equations. Recently, Ewing *et al.* (2007) extended the SP analysis to the governing equations for two-point correlations of velocity fluctuations in a temporally evolving plane wake. They found that the two-point correlation functions can collapse at all scales of motion using a single set of similarity variables. Ewing *et al.* (2007) adopted George's approach and assumed a general SP where several velocity scales and one length scale was considered. The analysis showed that the scaling velocity for the correlation, $\overline{u(t)v(t+\mathrm{d}t)}$ (the overbar denotes time averaging, and u and v are the streamwise (x) and normal (y) components of the velocity fluctuations, respectively), is $q_o = (u_o(\mathrm{d}\delta/\mathrm{d}t))^{1/2}$, while it is u_o for all the others (δ is the scaling length and t is time). Interestingly, Ewing *et al.* (2007) found $\delta \sim t^{1/2}$, which, since they also obtained $u_o \sim \delta^{-1}$, leads to Townsend's result, i.e. $u_o \sim q_o$. While the approach taken by Ewing *et al.* (2007) is valid for a temporally evolving wake, it cannot be directly applied to a spatially evolving flow as the equations of motion differ (unless some assumptions are made, for example the velocity defect is very weak).

In the present work, we apply a two-point SP analysis to a spatially evolving wake of a circular cylinder. We aim to extend the SP analysis of Townsend (1956) to two-point statistics, which is likely to provide a deeper insight into the flow details. As stated above, since the experimental evidence indicates that SP is reached in the far wake, the analysis will focus on the far wake. This flow region has received a significant amount of attention (e.g. Antonia & Browne 1986; Browne & Antonia 1986; Antonia *et al.* 1987; Browne, Antonia & Shah 1987; Antonia, Browne & Shah 1988; Bisset, Antonia & Browne 1990*b*; Bisset, Antonia & Britz 1990*a*; Brown & Roshko 2012). The present two-point SP analysis is applied on the transport equation of the second-order velocity structure function, $\overline{(\Delta u)^2}$, where $(\Delta u) = u(t, x) - u(t, x + r)$, with r being the longitudinal space increment; this equation is often referred to as a scale-by-scale (hereafter denoted s.b.s.) energy budget. Burattini, Antonia & Danaila (2005) applied such an analysis to the far field of a round jet. They claimed that the far field of a round jet is in an exact SP state because the Taylor microscale Reynolds number $Re_\lambda = u'\lambda/\nu$, based on the Taylor microscale λ and the root mean square (r.m.s.) of the streamwise velocity fluctuations u', is constant. This constancy follows from the SP analysis of the s.b.s. energy budget equation, but also from the assumption that $C_\epsilon = \overline{\epsilon} L_u/u'^3 = \text{const.}$ (L_u is the integral length scale). This assumption would also lead to $Re_\lambda = \text{const.}$ in the far wake, i.e. the far wake should also approach exact SP. This expectation has yet to be verified experimentally and by carrying out a two-point statistical analysis similar to that used by Burattini *et al.* (2005) in the far field of a round jet. This verification is the major objective of this paper. We emphasise that the assumption $C_\epsilon = \text{const.}$ is not essential for deriving $Re_\lambda = \text{const.}$ Self-preservation analysis of the s.b.s. energy

https://doi.org/10.1017/jfm.2015.663 Published online by Cambridge University Press

budget equation, i.e. a budget for each scale ranging from the smallest (smaller than the Kolmogorov length scale) to the largest scale (exceeding the integral length scale), is sufficient for this purpose in the far wake.

Since the pioneering work of Kolmogorov (1941), the turbulent energy dissipation rate, $\overline{\epsilon}$, is considered to be a cornerstone quantity in the study of turbulence, especially in the context of the small-scale motion (SSM). Batchelor & Townsend (1947) and Townsend (1951) measured moments of first- and higher-order spatial derivatives of the longitudinal velocity fluctuation u to characterise the behaviour of the SSM in decaying turbulence downstream of a grid. We recall here that a reliable estimation of the mean energy dissipation rate is a challenging task for the experimentalist. We will show that one important consequence of the SP analysis of the s.b.s. energy budget equation in the far wake is that it provides a simple means for estimating $\overline{\epsilon}$.

This paper is structured as follows. In § 2 we apply the SP analysis to the mean momentum equation and the s.b.s. energy budget equation in the far wake. Experimental details are presented in § 3. The SP analytical results are tested and discussed in both §§ 4 and 5. In § 4 we examine the single-point statistics (e.g. the downstream evolution of the mean velocity, Reynolds stress, λ, $\overline{\epsilon}$ and Re_λ, etc.), while in § 5 we focus on the two-point statistics (i.e. structure functions and spectra). Conclusions are given in § 6.

2. Equilibrium similarity analysis in the far wake

2.1. *Mean flow SP analysis*

We begin by applying the SP analysis to a steady-state two-dimensional turbulent wake for which the mean momentum equation in the streamwise direction is given by

$$U\frac{\partial U}{\partial x}+V\frac{\partial U}{\partial y}+\frac{\partial \overline{uv}}{\partial y}+\frac{\partial(\overline{u^2}-\overline{v^2})}{\partial x}=\nu\frac{\partial^2 U}{\partial y^2}. \tag{2.1}$$

Here, U, V are the streamwise (x-direction) and lateral (y-direction) components of the mean velocity respectively; $\overline{u^2}$, $\overline{v^2}$ and $\overline{uv}$ are the streamwise, lateral and shear stresses respectively. Following Townsend (1956), we assume

$$U_\infty - U = u_0 f(y^*), \tag{2.2a}$$
$$\overline{u^2} = v_0^2 g_u(y^*), \tag{2.2b}$$
$$\overline{v^2} = v_0^2 g_v(y^*), \tag{2.2c}$$
$$\overline{uv} = v_0^2 g_{uv}(y^*), \tag{2.2d}$$

where U_∞ is the free stream velocity, u_0 and v_0 are scaling velocities which depend on x and are not necessary identical, $y^*=y/l$, l being a scaling length which depends only on x. The functions f, g_u, g_v and g_{uv} are functions of y^* only. Substituting expressions (2.2) into (2.1) and using the continuity equation ($\boldsymbol{\nabla}\cdot U=0$) to solve for V, leads, after some trivial manipulations, to

$$-U_\infty\frac{\mathrm{d}u_0}{\mathrm{d}x}f+U_\infty\frac{u_0}{l}\frac{\mathrm{d}l}{\mathrm{d}x}\eta f'+u_0\frac{\mathrm{d}u_0}{\mathrm{d}x}f^2-\frac{u_0}{l}\frac{\mathrm{d}(u_0 l)}{\mathrm{d}x}f'\left\{\int_0^\eta f\,\mathrm{d}s\right\}$$
$$+\frac{v_0^2}{l}g'_{uv}+\frac{\mathrm{d}v_0^2}{\mathrm{d}x}(g_u-g_v)-\frac{v_0^2}{l}\frac{\mathrm{d}l}{\mathrm{d}x}\eta(g'_u-g'_v)=-\nu\frac{u_0}{l^2}f'', \tag{2.3}$$

https://doi.org/10.1017/jfm.2015.663 Published online by Cambridge University Press

where the prime and double prime denote first- and second-order derivatives with respect to y^* respectively. Multiplying all the terms of (2.3) by l/v_0^2 makes the coefficient of g'_{uv} equal to 1, and, accordingly, SP is satisfied if

$$\frac{U_\infty l}{v_0^2}\frac{\mathrm{d}u_0}{\mathrm{d}x} = C_1, \tag{2.4a}$$

$$U_\infty \frac{u_0}{v_0^2}\frac{\mathrm{d}l}{\mathrm{d}x} = C_2, \tag{2.4b}$$

$$\frac{u_0 l}{v_0^2}\frac{\mathrm{d}u_0}{\mathrm{d}x} = C_3, \tag{2.4c}$$

$$\frac{u_0}{v_0^2}\frac{\mathrm{d}(u_0 l)}{\mathrm{d}x} = C_4, \tag{2.4d}$$

$$1 = C_5, \tag{2.4e}$$

$$\frac{l}{v_0^2}\frac{\mathrm{d}v_0^2}{\mathrm{d}x} = C_6, \tag{2.4f}$$

$$\frac{\mathrm{d}l}{\mathrm{d}x} = C_7, \tag{2.4g}$$

$$\frac{\nu u_0}{v_0^2 l} = C_8, \tag{2.4h}$$

where the constants C_i $(i = 1 \ldots 8)$ are independent of x. Solving (2.4g) yields

$$l = C_7(x - x_0), \tag{2.5}$$

where we assumed that $l = 0$ when $x = x_0$; x_0 is a virtual origin. However, by considering the ratio C_2/C_8, we obtain

$$l = C(x - x_0)^{1/2}. \tag{2.6}$$

Clearly, (2.5) and (2.6) cannot be satisfied simultaneously.

Substituting (2.4g) into (2.4b), we have

$$v_0^2 = \frac{C_7}{C_2} U_\infty u_0. \tag{2.7}$$

Moreover, from (2.4b) alone, we obtain

$$v_0^2 = \frac{1}{C_2} U_\infty u_0 \frac{\mathrm{d}l}{\mathrm{d}x}. \tag{2.8}$$

We can also have an SP constraint on u_0 by taking the ratio between (2.4a) and (2.4c). This leads to

$$\frac{U_\infty}{u_0} = \frac{C_1}{C_3}. \tag{2.9}$$

Now, combining (2.7) and (2.9) yields

$$v_0^2 = \frac{C_7 C_1}{C_2 C_3} u_0^2. \tag{2.10}$$

Then, substituting (2.10) into (2.4h) leads to

$$\frac{u_0 l}{\nu} = Re_l = \text{constant}. \tag{2.11}$$

https://doi.org/10.1017/jfm.2015.663 Published online by Cambridge University Press

Some discussion is required at this stage of the analysis. We note that the condition (2.8) is similar to that of George (1989) for the Reynolds stress velocity scale. One can see that this constraint will also apply to a turbulent boundary layer, a jet flow and a mixing layer since the mean momentum in these flows obeys the same equation (2.1), which Townsend (1956, 1976) used as the foundation for his SP analysis of different turbulent flows. In his analysis, George (1989) only considered a first-order approximation form of (2.1) where the second and fourth terms of the left-hand side as well as the term on the right-hand side are removed. The approximation further assumes that $U \simeq U_\infty$, and thus the first term of (2.1) can be replaced by $U_\infty(\partial U/\partial x)$. This then removes the SP constraints (2.4*d*), (2.4*f*–*h*) from the analysis. It is believed that the first-order approximation of the mean momentum equation is valid in the far wake where the defect velocity can be considered to be very small, leading to $U \simeq U_\infty$. Townsend (1956) proposed that if $U_\infty/u_0 \gg f$ in (2.3) then SP is possible in the plane wake. This condition leads to $C_1 \gg C_3$ and, since $U_\infty u_0\, \mathrm{d}l/\mathrm{d}x = u_o\, \mathrm{d}(U_\infty l)/\mathrm{d}x$, $C_2 \gg C_4$, and accordingly the third and fourth terms on the left-hand side of (2.3) can be dropped. Townsend (1956) further assumed that the sixth, seventh and eighth terms can be neglected. At this stage of the analysis we do not make such simplifications.

It is worthwhile to comment on the consequence of dropping terms from (2.1). First, let us consider dropping the right-hand side, which, in effect, amounts to dropping the SP condition (2.4*h*). This can only lead to the solution (2.5). If we drop the fourth term on the left-hand side of (2.1) and retain the right-hand side, SP solution (2.6) is obtained. If these terms are dropped (George 1989), one cannot predict the streamwise evolution of l based on the mean momentum equation alone and is left with constraint (2.8). George (1989) obtained this evolution by considering the momentum integral to first order, i.e. by assuming that the momentum integral is constant.

In the next section we apply the SP analysis to the s.b.s. energy budget, which will help us to obtain the appropriate streamwise evolution of l.

2.2. *Scale-by-scale SP analysis*

According to Danaila *et al.* (2001), the s.b.s. energy budget equation on the axis of a plane far wake is given by

$$-\frac{1}{r^2}\int_0^r s^2\left[U\frac{\partial\overline{(\Delta u_i)^2}}{\partial x}\right]\mathrm{d}s+\frac{2}{r^2}\int_0^r s^2\left[-\frac{\partial\overline{u_2(\Delta u_i)^2}}{\partial y}\right]\mathrm{d}s$$
$$-\overline{\Delta u_1(\Delta u_i)^2}+2\nu\frac{\partial}{\partial r}\overline{(\Delta u_i)^2}=\frac{4}{3}\bar{\epsilon}r, \tag{2.12}$$

where s is a dummy variable, identifiable with the separation along x; the u_i ($i = 1, 2, 3$) represent the velocity fluctuations in the x, y and z directions respectively. In this paper, u_1, u_2 and u_3 will be used interchangeably with u, v, w; similarly for x_1, x_2, x_3 and x, y, z. The first and second terms on the left-hand side of (2.12) are the large-scale forcing terms which arise from the transport of $(\Delta u_i)^2$ by the mean velocity U and the lateral velocity fluctuation u_2, namely convection and turbulent diffusion respectively. The third term in (2.12) is the generalised third-order structure function (representing energy transfer between scales), while the fourth term represents the viscous diffusion. The term on the right-hand side of (2.12) is proportional to the energy dissipation rate and balances the sum of the other terms. Applying the limit at $r \to \infty$ yields the one-point kinetic energy budget, namely

$$\frac{1}{2}U\frac{\partial\overline{q^2}}{\partial x}+\frac{\partial}{\partial y}\left(\frac{1}{2}\overline{u_2q^2}\right)+\bar{\epsilon}=0. \tag{2.13}$$

https://doi.org/10.1017/jfm.2015.663 Published online by Cambridge University Press

We examine the conditions under which (2.12) satisfies SP at all scales by assuming the following functional forms for the terms in this equation:

$$\left.\begin{aligned}\overline{\Delta u_i^2} &= u^{*2} f(\xi, \zeta),\\ -\overline{u_2 \Delta u_i^2} &= u^{*3} e(\xi, \zeta),\\ -\overline{\Delta u_1 \Delta u_i^2} &= u^{*3} g(\xi, \zeta),\end{aligned}\right\} \tag{2.14}$$

where $\xi = r/l$, $\zeta = y/\delta$; l and δ are characteristic length scales in the r and y directions respectively; u^* is a characteristic velocity scale. It should be noted that we assume only one velocity scale. Moreover, we do not presume any SP form for $\overline{\epsilon}$. The dimensionless functions $f(\xi, \zeta)$, $e(\xi, \zeta)$ and $g(\xi, \zeta)$ may depend on the initial conditions and are not considered here. After substituting expressions (2.14) into (2.12), we obtain the following SP s.b.s. equation:

$$-\frac{U}{r^2}\frac{\mathrm{d}u^{*2}}{\mathrm{d}x} l^3 \Gamma_1 + \frac{Uu^{*2}}{r^2}\frac{\mathrm{d}l}{\mathrm{d}x} l^2 \Gamma_2 + \frac{2u^{*3}}{\delta r^2} l \Gamma_3 + u^{*3} g(\xi, \zeta) + 2\nu u^{*2} \frac{1}{l}\frac{\mathrm{d}f(\xi, \zeta)}{\mathrm{d}\xi} = \frac{4}{3}\overline{\epsilon} r, \tag{2.15}$$

where

$$\left.\begin{aligned}\Gamma_1 &= \int_0^{r/l} \frac{s^2}{l^2} f(\xi, \zeta)\, \mathrm{d}\left(\frac{s}{l}\right),\\ \Gamma_2 &= \int_0^{r/l} \frac{s^3}{l^3}\frac{\mathrm{d}f(\xi, \zeta)}{\mathrm{d}\xi}\, \mathrm{d}\left(\frac{s}{l}\right),\\ \Gamma_3 &= \int_0^{r/l} \frac{s^2}{l^2}\frac{\mathrm{d}e(\xi, \zeta)}{\mathrm{d}\zeta}\, \mathrm{d}\left(\frac{s}{l}\right).\end{aligned}\right\} \tag{2.16}$$

It should be noted that the relations

$$\left.\begin{aligned}\frac{\partial \xi}{\partial x} &= -r l^{-2}\frac{\mathrm{d}l}{\mathrm{d}x},\\ \frac{\partial \zeta}{\partial y} &= \frac{1}{l}\end{aligned}\right\} \tag{2.17}$$

have been used in deriving (2.15). After multiplication by $(l/\nu u^{*2})$, (2.15) becomes

$$\begin{aligned}&-\left[\frac{Ul^2}{\nu u^{*2}}\frac{\mathrm{d}u^{*2}}{\mathrm{d}x}\right]\frac{\Gamma_1}{\xi^2} + \left[\frac{Ul}{\nu}\frac{\mathrm{d}l}{\mathrm{d}x}\right]\frac{\Gamma_2}{\xi^2} + \left[\frac{2u^* l^2}{\nu\delta}\right]\frac{\Gamma_3}{\xi^2}\\ &+\left[\frac{u^* l}{\nu}\right] g(\xi, \zeta) + [2]\frac{\mathrm{d}f(\xi, \zeta)}{\mathrm{d}\xi} = \left[\frac{4}{3}\frac{\overline{\epsilon} l^2}{\nu u^{*2}}\right]\xi.\end{aligned} \tag{2.18}$$

If we express the mean velocity in terms of U_∞ and the defect velocity U_d, $U = U_\infty - U_d$, (2.18) becomes

$$\begin{aligned}&-\left[\frac{U_\infty l^2}{\nu u^{*2}}\frac{\mathrm{d}u^{*2}}{\mathrm{d}x}\right]\frac{\Gamma_1}{\xi^2} + \left[\frac{U_\infty l}{\nu}\frac{\mathrm{d}l}{\mathrm{d}x}\right]\frac{\Gamma_2}{\xi^2} + \left[\frac{U_d l^2}{\nu u^{*2}}\frac{\mathrm{d}u^{*2}}{\mathrm{d}x}\right]\frac{\Gamma_1}{\xi^2} - \left[\frac{U_d l}{\nu}\frac{\mathrm{d}l}{\mathrm{d}x}\right]\frac{\Gamma_2}{\xi^2}\\ &+\left[\frac{2u^* l^2}{\nu\delta}\right]\frac{\Gamma_3}{\xi^2} + \left[\frac{u^* l}{\nu}\right] g(\xi, \zeta) + [2]\frac{\mathrm{d}f(\xi, \zeta)}{\mathrm{d}\xi} = \left[\frac{4}{3}\frac{\overline{\epsilon} l^2}{\nu u^{*2}}\right]\xi.\end{aligned} \tag{2.19}$$

https://doi.org/10.1017/jfm.2015.663 Published online by Cambridge University Press

For SP, all of the terms within square brackets must evolve in the streamwise direction in exactly the same way. Since the last term on the left-hand side of (2.19) is constant, all of the others must also be constant, namely

$$\frac{U_\infty l^2}{\nu u^{*2}}\frac{\mathrm{d}u^{*2}}{\mathrm{d}x} = C_1, \tag{2.20a}$$

$$\frac{U_\infty l}{\nu}\frac{\mathrm{d}l}{\mathrm{d}x} = C_2, \tag{2.20b}$$

$$\frac{U_d l^2}{\nu u^{*2}}\frac{\mathrm{d}u^{*2}}{\mathrm{d}x} = C_3, \tag{2.20c}$$

$$\frac{U_d l}{\nu}\frac{\mathrm{d}l}{\mathrm{d}x} = C_4, \tag{2.20d}$$

$$\frac{u^* l^2}{\nu\delta} = C_5, \tag{2.20e}$$

$$\frac{u^* l}{\nu} = C_6, \tag{2.20f}$$

$$\frac{\bar{\epsilon} l^2}{\nu u^{*2}} = C_7. \tag{2.20g}$$

Equation (2.20*f*) indicates that in the far wake, the Reynolds number, based on the characteristic length and velocity scales (u^* and l), must remain constant.

The ratios of (2.20*c*) to (2.20*a*) and (2.20*d*) to (2.20*b*) lead to

$$\frac{C_3}{C_1} = \frac{C_4}{C_2} = \frac{U_d}{U_\infty}, \tag{2.21}$$

i.e. U_d/U_∞ must be constant for SP to be reached. However, since U_d decreases as x/d increases, one expects that $U_d/U_\infty \to 0$ as $x/d \to \infty$. It is then reasonable to expect that $U_d/U_\infty \simeq 0$ beyond some downstream distance, such as in the far wake. In that case, C_3 and C_4 become negligible compared with C_1 and C_2, and constraints (2.20*c*) and (2.20*d*) are no longer relevant and can be dropped from the analysis. Then, (2.20*b*) leads to the following expression for the characteristic length scale l:

$$\frac{l}{d} = c_1\left(\frac{x}{d} - \frac{x_0}{d}\right)^{1/2}, \tag{2.22}$$

where x_0 is the effective flow origin and c_1 is a constant prefactor.

Equations (2.20*a*) and (2.20*g*) show that u^* and $\bar{\epsilon}$ should behave as

$$\frac{u^*}{U_\infty} = c_2\left(\frac{x}{d} - \frac{x_0}{d}\right)^{-1/2} \tag{2.23}$$

and

$$\frac{\bar{\epsilon} d}{U_\infty^3} = c_\epsilon\left(\frac{x}{d} - \frac{x_0}{d}\right)^{-2}. \tag{2.24}$$

It should be noted that (2.22)–(2.24) have been normalised by d and U_∞. Equation (2.20*e*) suggests that the characteristic length scale δ behaves like l, namely

$$\frac{\delta}{l} = \text{const.} \tag{2.25}$$

If one selects the half-width of the far wake, L_0, as representing δ, then one expects $L_0 \sim x^{1/2}$.

https://doi.org/10.1017/jfm.2015.663 Published online by Cambridge University Press

A number of comments can be made based on the SP analyses shown above.

(i) Strictly, SP is reached exactly when the velocity defect U_d is zero, which is likely to occur when $x/d \to \infty$. However, if there is a region where $U_d \ll U_\infty$, then SP solutions can be attained at some finite distance downstream of the cylinder. This is likely to occur in the far-wake region.

(ii) Equation (2.25) implies that $\delta \sim x^{1/2}$, which shows that the SP constraint (2.4*g*) on the mean momentum equation is not applicable, or, equivalently, the last term on the left-hand side of (2.3) is negligible and can be dropped from the SP analysis. It should be noted that this is different from dropping the fourth term on the left-hand side of (2.1).

(iii) Forming the ratio of (2.4*c*) and (2.4*a*) leads to u_o/U_∞. Townsend (1956, 1976) assumed this ratio to be negligible and further dropped constraints (2.4*f*–*h*), which amounts to using the first-order mean momentum equation,

$$U\frac{\partial U}{\partial x} + V\frac{\partial U}{\partial y} = -\frac{\partial \langle uv \rangle}{\partial y}, \tag{2.26}$$

commonly used in the far wake. It should be noted that if one uses the Taylor hypothesis ($x = Ut$) to convert space to time, then one obtains the temporally evolving plane wake. It appears that these simplifications are too restrictive. For example, there is no compelling justification for dropping the viscous term (e.g. the right-hand side term of (2.1)). In fact, retaining it leads, as seen in § 2.1, to the important constraint $Re_l = u_0 l/\nu = \text{constant}$, which is consistent with the SP constraint (2.20*f*) applied to the s.b.s. budget.

(iv) If l is identified with λ and u^* with u', then $Re_\lambda = \text{const}$. This is a convenient test for SP since Re_λ is a relatively straightforward quantity to measure.

(v) Combining (2.20*e*) and (2.20*g*) yields

$$\frac{\bar{\epsilon} l}{u^{*3}} = C_8. \tag{2.27}$$

If $l = L$ is the integral length scale and $u_* = u'$, then we obtain $C_8 = C_\epsilon = \text{constant}$, revealing that the constancy of C_ϵ is simply a consequence of SP.

We now follow the work of Thiesset, Antonia & Djenidi (2014) and derive an exact expression for $\bar{\epsilon}$ using the SP solutions of the s.b.s. budget equation. As seen above, SP is reached when the defect velocity is negligible, which we assume at this stage to be well verified in the far wake. We thus focus the analysis on the far wake and seek to write the transport equation for the average kinetic energy ($\overline{q^2} = \overline{u_i^2}$) along the axis of the far wake. Several attempts have been made to measure the various terms of (2.13) in the far wake. For example, Browne *et al.* (1987), Aronson & Lofdahl (1993) and Lefeuvre *et al.* (2014) showed that, on the centreline of the far wake, the advection and diffusion terms (the first and second terms in (2.13) respectively) contribute significantly to the budget. Further, they found that the diffusion and advection terms are approximately equal, i.e.

$$\frac{\partial \overline{vq^2}}{\partial y} \approx U\frac{\partial \overline{q^2}}{\partial x}. \tag{2.28}$$

Equation (2.13) can then be rewritten as

$$U\frac{\partial \overline{q^2}}{\partial x} + \bar{\epsilon} \approx 0. \tag{2.29}$$

https://doi.org/10.1017/jfm.2015.663 Published online by Cambridge University Press

The turbulent kinetic energy along the axis of the far wake can be approximated by

$$\overline{q^2} = \overline{u_1^2} + 2\overline{u_2^2} = \overline{u_1^2}(1+2R), \tag{2.30}$$

where $R = \overline{u_2^2}/\overline{u_1^2}$, which represents a measure of large-scale anisotropy; the approximation $u_2^2 \simeq u_3^2$ was used. This approximation is well supported by the measurements of Hao *et al.* (2008) on the centreline of the far wake, where it was shown that $\overline{u_1^2}/\overline{u_2^2} \simeq \overline{u_1^2}/\overline{u_3^2} \simeq 1.4$ at $R_d = U_\infty d/\nu = 2000$. After substituting (2.24) and (2.30) in (2.29), we obtain

$$\frac{\overline{u^2}}{U_\infty^2} = \frac{c_\epsilon}{(1+2R)}\left(\frac{x-x_0}{d}\right)^{-1} = A_u^2\left(\frac{x-x_0}{d}\right)^{-1}, \tag{2.31}$$

where A_u is a power-law prefactor for u'. It should be noted that the condition that U_d/U_∞ is negligible (see (2.21)) is also used in deriving (2.31), since we are focusing on the far wake.

Combining (2.31) with (2.24) yields an expression for $\bar{\epsilon}$, namely

$$\frac{\bar{\epsilon} d}{U_\infty^3} = c_\epsilon\left(\frac{x}{d} - \frac{x_0}{d}\right)^{-2} = A_u^2(1+2R)\left(\frac{x}{d} - \frac{x_0}{d}\right)^{-2}. \tag{2.32}$$

This expression provides a relatively simple method for estimating $\bar{\epsilon}$, whose reliable measurement represents a challenge to the experimentalist. Indeed, it is sufficient to measure $\overline{u^2}$ and R in order to estimate $\bar{\epsilon}$.

It should be remembered that the departure from local isotropy in the far-wake region is not negligible, even on the flow centreline where the mean shear is zero (e.g. Antonia & Browne 1986; Browne *et al.* 1987). This departure can be quantified as follows:

$$R_\epsilon = \frac{\bar{\epsilon}_{iso}}{\bar{\epsilon}}. \tag{2.33}$$

Accordingly, (2.32) can be written as

$$\frac{\bar{\epsilon}_{iso} d}{U_\infty^3} = R_\epsilon c_\epsilon\left(\frac{x}{d} - \frac{x_0}{d}\right)^{-2} = A_u^2 R_\epsilon(1+2R)\left(\frac{x}{d} - \frac{x_0}{d}\right)^{-2}. \tag{2.34}$$

It follows that the Kolmogorov velocity and length scales (u_K, η) should behave as

$$\frac{u_K}{U_\infty} = \left[\frac{A_u^2 R_\epsilon(1+2R)}{R_d}\right]^{1/4}\left(\frac{x}{d} - \frac{x_0}{d}\right)^{-1/2}, \tag{2.35}$$

$$\frac{\eta}{d} = [R_d^3 R_\epsilon A_u^2(1+2R)]^{-1/4}\left(\frac{x}{d} - \frac{x_0}{d}\right)^{1/2}, \tag{2.36}$$

leading to

$$\overline{u^{*2}} = \frac{\overline{u^2}}{u_K^2} = \left[\frac{A_u^2 R_d}{(1+2R)R_\epsilon}\right]^{1/2}, \tag{2.37}$$

which is constant. Since $\overline{u^{*2}} = Re_\lambda/\sqrt{15}$, it follows that

$$A_{Re_\lambda} = \frac{Re_\lambda}{R_d{}^{1/2}} = \left[\frac{15A_u^2}{(1+2R)R_\epsilon}\right]^{1/2}. \tag{2.38}$$

https://doi.org/10.1017/jfm.2015.663 Published online by Cambridge University Press

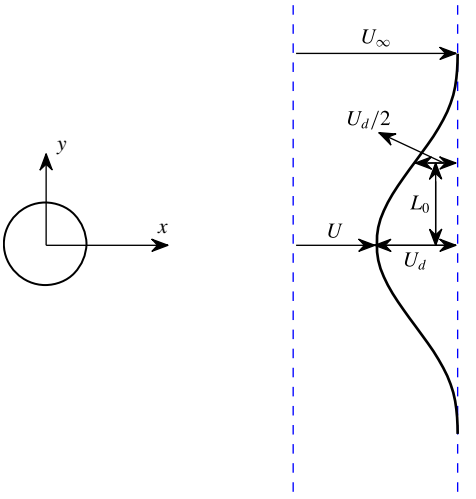

FIGURE 1. (Colour online) Schematic arrangement and coordinate axis. Here, U is the mean velocity; U_∞ is the free stream velocity; U_d is the maximum velocity defect; L_0 is the half-width of the wake. It should be noted that U and U_d are arbitrarily shown on the centreline.

Using the definition of the Taylor microscale λ leads to

$$\frac{\lambda^2}{d^2} = \frac{15\nu\overline{u^2}}{\overline{\epsilon}_{iso}d^2} = \frac{15}{R_d(1+2R)R_\epsilon}\left(\frac{x}{d} - \frac{x_0}{d}\right) = A_\lambda^2\left(\frac{x}{d} - \frac{x_0}{d}\right) \tag{2.39}$$

and

$$\lambda^* = \frac{\lambda}{\eta} = \left[\frac{15^2 R_d A_u^2}{(1+2R)R_\epsilon}\right]^{1/4}, \tag{2.40}$$

which is constant.

Similarly to the analysis of Thiesset *et al.* (2014), the present SP analysis, applied to the s.b.s. budget equation, allows one to derive exact expressions for $\overline{u}^2$, $\overline{\epsilon}$ and all subsequent quantities. In particular, relationships between the prefactors A_u, A_λ, A_{Re_λ} and c_ϵ ensue. All of the results derived from the equilibrium similarity of the far wake are tested in §§ 4 and 5.

3. Experimental details

Experiments were carried out in a non-return blower-type wind tunnel with a square cross-section (350 mm × 350 mm) of 2.4 m in length. The inclination of the bottom wall of the working section was adjusted in order to maintain a zero streamwise pressure gradient. The wake was generated by a cylinder ($d = 3$ mm), installed horizontally in the midplane and spanning the full width of the working section (figure 1) and located 10 cm downstream of the exit plane of the contraction. This resulted in a blockage of approximately 0.9 % and an aspect ratio of 175. The free steam velocity U_∞ was 10.6 m s^{-1} and the corresponding Re_d was 2000. At this Reynolds number, the background turbulence intensity, u'/U_∞, is at most approximately 0.3 %. The measurement locations ranged from the intermediate wake ($x/d = 20$) to the far wake ($x/d = 600$).

https://doi.org/10.1017/jfm.2015.663 Published online by Cambridge University Press

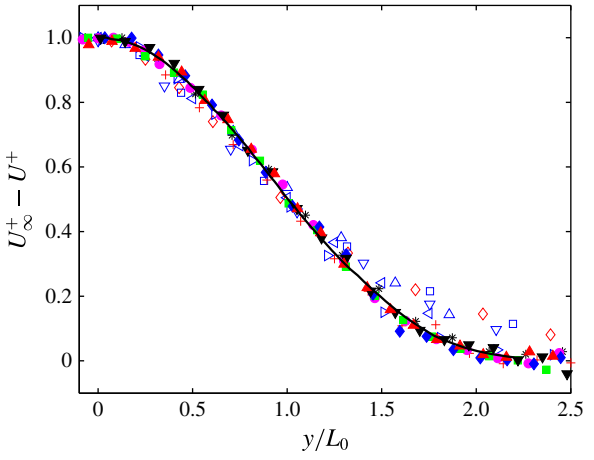

FIGURE 2. (Colour online) Normalised mean velocity defect at $Re_d = 2000$, for $x/d =$ ◇, 20; □, 40; ▽, 60; △, 80; ◁, 100; ▷, 170; ∗, 211; •, 277; ●, 344; ■, 401; ◆, 468; ▼, 534; ▲, 601. The solid curve corresponds to the cylinder far wake at $x/d = 420$ (Browne *et al.* 1987).

The measurements were carried out using hot-wire anemometry. The Wollaston (Pt–10 % Rh) hot wire (diameter $d_w = 2.5$ μm) was etched to an active length of approximately $l_w = 0.5$ mm. The length to diameter ratio of the wires was typically 200. The hot wire was operated with constant-temperature anemometers at an overheat ratio of 1.5. The output signals from the anemometers were passed through buck and gain circuits and low-pass filtered (the cutoff frequency f_c, which was in the range 6300–12 500 Hz depending on the transverse position of the probe, was set close to the Kolmogorov frequency $f_\eta = U/2\pi\eta$). The signal was then digitised into a personal computer using a 12 bit analogue-to-digital (A/D) converter at a sampling frequency in the range 12 600–25 000 Hz. The recording duration, which varied between 100 and 140 s, was long enough for the second- and third-order moments to converge on the basis of criteria proposed by Anselmet *et al.* (1984) and Camussi & Guj (1995).

4. Test of equilibrium similarity: single-point statistics

4.1. *Mean velocity and Reynolds stresses*

Constraints (2.9) and (2.21) show that one can use $u_0 = U_d$. Thus, the mean velocity defect $U_\infty^+ - U^+$, normalised with U_d and L_0, is shown in figure 2. Also shown are the data of Browne *et al.* (1987) at $x/d = 420$. There is a reasonable collapse of the distributions for $U_\infty^+ - U^+$ in the range $x/d > 100$ between the present data and those of Browne *et al.* (1987). As pointed out by Zhou & Antonia (1995), the distributions for $(U_\infty^+ - U^+)$ are approximately independent of the wake generators in the far-wake region of the plane wakes, although discernible differences can be observed in the Reynolds stresses, spectra of v and vorticities. For $x/d < 100$, discernible differences can be observed, especially near the outer edge of the wake. This is also consistent with the observations of Antonia & Mi (1998) in the range $x/d \leqslant 70$.

The r.m.s. of the streamwise fluctuations u_{rms}^+, normalised with U_d and L_0, is shown in figure 3. Antonia & Mi (1998) reported that the magnitude of u_{rms}^+ decreases as x/d increases over the range $x/d = 10$–70. The same can be observed in figure 3.

https://doi.org/10.1017/jfm.2015.663 Published online by Cambridge University Press

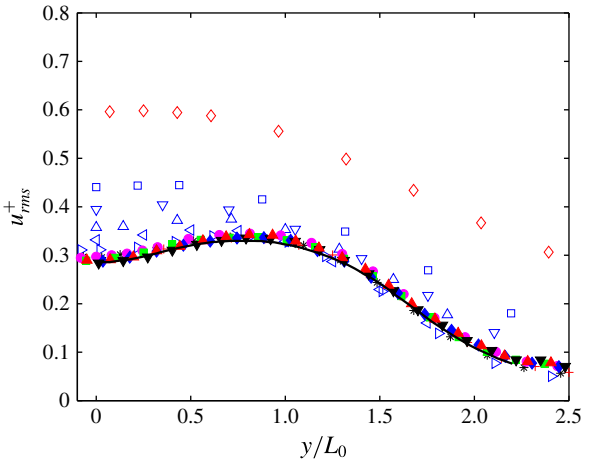

FIGURE 3. (Colour online) Normalised r.m.s. longitudinal velocity at $Re_d = 2000$, for $x/d =$ ◇, 20; □, 40; ▽, 60; △, 80; ◁, 100; ▷, 170; ∗, 211; •, 277; ●, 344; ■, 401; ◆, 468; ▼, 534; ▲, 601. The solid curve corresponds to the cylinder far wake at $x/d = 420$ (Browne *et al.* 1987).

More importantly, the magnitude of u^+_{rms} keeps decreasing as x/d increases, eventually reaching a constancy beyond $x/d \approx 200$. This suggests that SP is satisfied closely for $x/d > 200$, at least in the context of Reynolds stresses.

4.2. *Streamwise variation of scaling parameters*

The scaling parameters, U_d and L_0, clearly provide the collapse of the mean velocity profiles and the r.m.s. longitudinal velocity, as shown in figures 2 and 3. From the s.b.s. SP analysis, we show that any velocity scale must decay as $x^{-1/2}$ whereas any length scale must grow as $x^{1/2}$. For U_d and L_0, namely

$$\frac{U_d}{U_\infty} = C_1 \left[\frac{x - x_0}{d}\right]^{-1/2}, \tag{4.1}$$

$$\frac{L_0}{d} = C_2 \left[\frac{x - x_0}{d}\right]^{1/2}. \tag{4.2}$$

The streamwise variations of U_d and L_0 are shown in figure 4. A least-squares linear fit has been applied to the distributions of $(U_\infty/U_d)^2$ and $(L_0/d)^2$ over the range $x/d = 260$–600. It is clear that the present data support the results from the above s.b.s. SP analysis over the range $x/d > 260$, where both $(U_\infty/U_d)^2$ and $(L_0/d)^2$ grow linearly. The estimated values for C_1 and C_2, which are 1.11 and 0.21 respectively, are in good agreement with those of Wygnanski *et al.* (1986) ($C_1 = 1.24$ and $C_2 = 0.20$), Browne & Antonia (1986), Browne *et al.* (1987) ($C_1 = 1.28$ and $C_2 = 0.20$) and Aronson & Lofdahl (1993) ($C_1 = 1.25$ and $C_2 = 0.20$), although they may depend on the initial conditions, as reported by (Wygnanski *et al.* 1986). Interestingly, there is also a linear evolution for both $(U_\infty/U_d)^2$ and $(L_0/d)^2$ over the range $x/d = 20$–100 (a least-squares linear fit has also been applied over this range). This is consistent with Mi, Zhou & Nathan (2004). Indeed over the range $x/d = 20$–100, both the mean temperature and the r.m.s. temperature on the wake axis decay as $x^{-1/2}$, while the

https://doi.org/10.1017/jfm.2015.663 Published online by Cambridge University Press

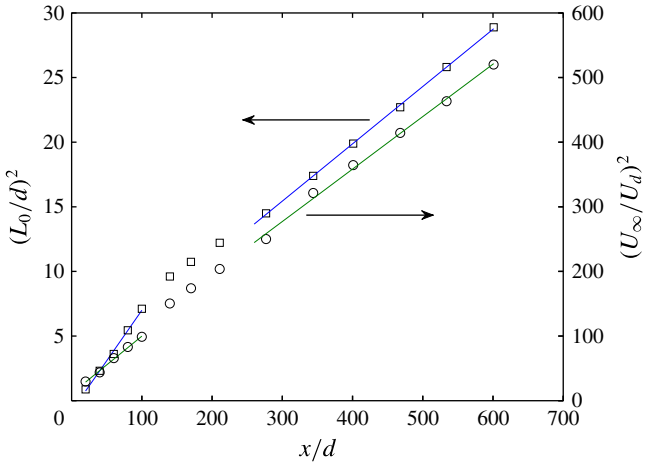

FIGURE 4. (Colour online) Downstream evolution of U_d and L_0 at $Re_d = 2000$. The solid lines are the linear fits over the ranges $x/d = 260$–600 and $x/d = 20$–100 respectively.

half-widths of the mean velocity and scalar fields grow as $x^{1/2}$. A linear evolution for $(U_\infty/U_d)^2$ and $(L_0/d)^2$ is also observed in a square cylinder wake over the range $x/d = 30$–100 (DNS data of Lefeuvre, private communication, 2014) at $Re_d = 2000$. Figure 4 shows that the rates of change with x of $(U_\infty/U_d)^2$ and $(L_0/d)^2$ are smaller in the far wake than over the range $x/d = 20$–100 (intermediate wake). This is more pronounced for $(L_0/d)^2$ than for $(U_\infty/U_d)^2$. The change of the rates from the ranges $x/d = 20$–100 to $x/d = 260$–600 seems to be an effect of the reorganisation or rescaling of the large-scale structures (Brown & Roshko 2012), which occurs over the range $x/d = 100$–260. This reorganisation or rescaling depends on the initial conditions. Figure 4 shows that the turbulent wake of a circular cylinder evolves through three stages, i.e. two linear evolution stages over the ranges $x/d = 20$–100 and 260–600, and a transition stage over the range $100 \leqslant x/d \leqslant 260$, where the upstream and downstream limits depend on the ICs. Moreover, based on the results for a circular cylinder, only two basic regions are recognised by Brown & Roshko (2012) over the range $4 \leqslant x/d \leqslant 1000$, namely the intermediate wake ($4 \leqslant x/d \leqslant 50$) and the far wake ($50 \leqslant x/d \leqslant 1000$). This different classification is, in essence, due to the fact that different criteria are used. Brown & Roshko (2012) showed that, in the intermediate wake, the presence of vortices shed from the cylinder is detectable, whereas in the far wake, there is approximately self-similar behaviour of the mean velocity, as shown in figure 2. The present classification is based on the streamwise evolution of the scaling parameters U_d and L_0. The transition region $100 \leqslant x/d \leqslant 260$ is certainly worthy of further investigation. A further worthwhile issue to be investigated is the effect of the individual contributions from the energetic coherent structures and the velocity defect on the establishment of SP in the far wake, in particular on the limit of validity of SP on x/d. Both of these features are dependent on the initial conditions. A possible way to assess the effects of the energetic coherent structures, which are likely to impact strongly on the wake flow evolution in the near-wake region, would be to systematically vary the Reynolds number for a given bluff body shape. The effect of the velocity defect could be assessed by varying the shape of the bluff body for a fixed Reynolds number, or, alternatively, by using a bluff body with different rear base bleeds. Interestingly, this latter approach amounts to assessing the effect of

https://doi.org/10.1017/jfm.2015.663 Published online by Cambridge University Press

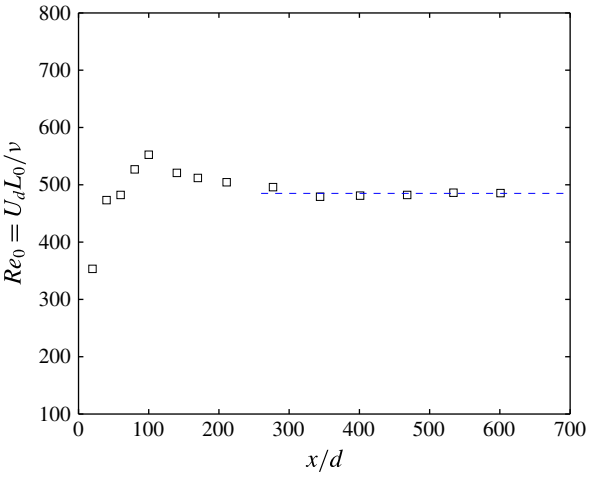

FIGURE 5. (Colour online) Downstream evolution of the local Reynolds number Re_0 at $Re_d = 2000$. The solid line is the mean value of Re_0 over the range $x/d = 260$–600.

the drag on the establishment of SP. However, since the velocity defect reflects the force drag, one must be careful when using the estimate of the drag based on the momentum integral for assessing the SP results. For example, estimates of the drag based on the first-order momentum integral (valid in the far wake only) will result in inconsistency with SP in regions where the velocity defect is not negligible, such as in the near-wake field.

The local Reynolds number based on U_d and L_0, $Re_0 = U_d L_0/\nu$, is shown in figure 5. As expected from the s.b.s. SP analysis, Re_0 is constant for $x/d > 260$. By contrast, although both $(U_\infty/U_d)^2$ and $(L_0/d)^2$ grow linearly over the range $x/d = 20$–100, Re_0 increases continuously instead of remaining constant. This is because different values of the virtual origin (x_0) apply to $(U_\infty/U_d)^2$ and $(L_0/d)^2$ over the range $x/d = 20$–100 (it is clear in figure 4 that there is an intersection at $x/d \approx 40$), whereas in the far wake, the values of x_0, estimated from $(U_\infty/U_d)^2$ and $(L_0/d)^2$, are approximately equal (this will be discussed in the next paragraph). Over the transition stage ($100 \leqslant x/d \leqslant 260$), Re_0 decreases continuously.

The streamwise variations of $(\lambda/d)^2$, $(U_\infty/u_{rms})^2$ and $(\eta/d)^2$ are shown in figures 6 and 7. All three quantities vary smoothly over the range $x/d = 20$–200, before increasing linearly for $x/d > 200$. The solid lines in figures 6 and 7 are linear fits over the range $x/d = 200$–600. Like the local Reynolds number Re_0 in figure 5, the Taylor microscale Reynolds number Re_λ, shown in figure 8, reaches a constant value beyond $x/d \simeq 200$, implying that SP is satisfied closely. Several further comments can be made with regard to figures 4–8.

(i) Self-preservation is achieved approximately in the far wake (beyond $x/d > 260$ for all statistics) of a circular cylinder, indicating that all length scales (L_0, λ, or η) and velocity scales (U_d, u_{rms} or u_K) behave similarly, i.e. all velocity scales decay as $x^{-1/2}$, whereas the length scales grow as $x^{1/2}$, or the Reynolds numbers, based on any characteristic set of length and velocity scales, are constant. This feature of the far-wake region allows one to use all of the length and velocity scales interchangeably when scaling the data, e.g. the energy structure functions and spectra collapse over the entire range of scales/wavenumbers when normalised by any set of length and velocity scales; this will be discussed in the next section.

https://doi.org/10.1017/jfm.2015.663 Published online by Cambridge University Press

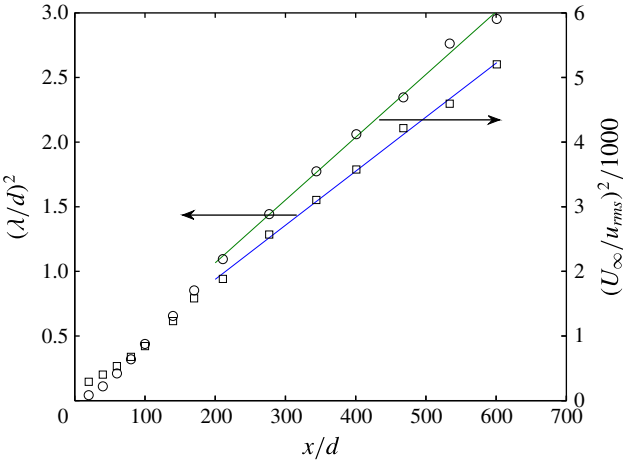

FIGURE 6. (Colour online) Downstream evolution of λ and u' at $Re_d = 2000$. The solid lines are the linear fits over the range $x/d = 200$–600.

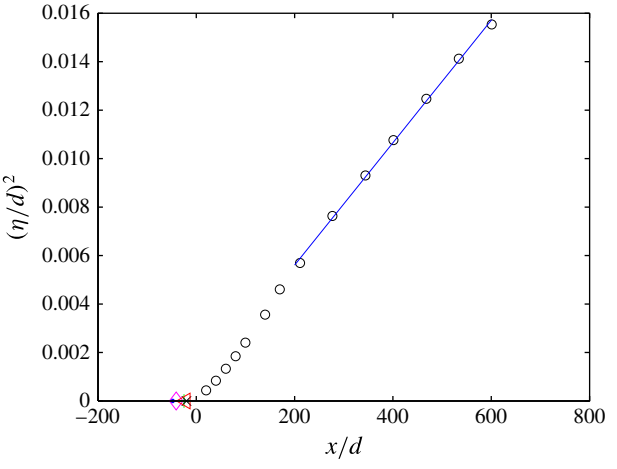

FIGURE 7. (Colour online) Downstream evolution of η at $Re_d = 2000$. The solid line is the linear fit over the range $x/d = 200$–600. For the purpose of comparison, we also show the values of x_0 for different quantities: $(U_\infty/U_d)^2$, $\diamond$; $(L_0/d)^2$, $\bullet$; $(\lambda/d)^2$, $+$; $(U_\infty/u_{rms})^2$, $\times$; $(\eta/d)^2$, $\triangleleft$.

(ii) As the flow evolves from the near-wake field to the far-wake field, the statistics associated with the large-scale motion (LSM) approach SP at a lower rate than those associated with the small-scale motion. This is reflected by the fact that Re_λ (see figure 8) reaches a constant faster than Re_0 (see figure 5). It is also reflected by the ratios of all length scales (i.e. L_0/η, λ/η and L_0/λ, not shown here) and all velocity scales (i.e. U_d/U_k, u_{rms}/U_K and U_d/u_{rms}, not shown). Namely, to become constant, the ratios associated with the large scales (i.e. L_0/η, L_0/λ, U_d/U_k and U_d/u_{rms}) require longer downstream distances than the ratios associated with the small scales (λ/η and u_{rms}/U_K).

https://doi.org/10.1017/jfm.2015.663 Published online by Cambridge University Press

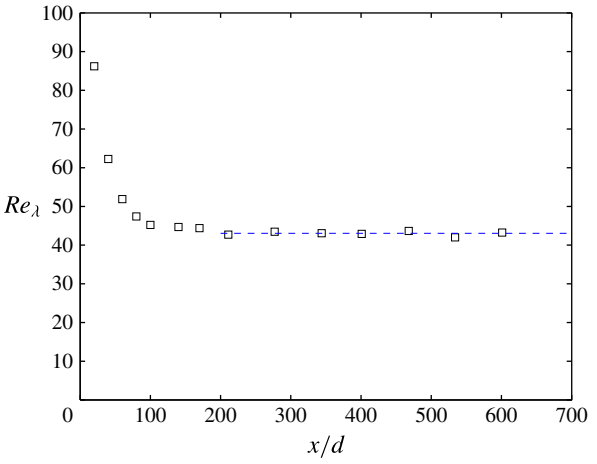

FIGURE 8. (Colour online) Downstream evolution of the Taylor Reynolds number Re_λ at $Re_d = 2000$. The solid line indicates the mean value of Re_λ over the range $x/d = 200$–600.

(iii) In the s.b.s. SP analysis we assumed that x_0 associated with the different length scales (L_0, λ, or η) and velocity scales (U_d, u_{rms} or u_K) is identical. To test this assumption, we marked the values of x_0 for all quantities in figure 7 at $Re_d = 2000$. They are approximately equal ($\approx -25d$). For comparison, we reproduce the values of x_o measured in other cylinder wakes and reported in the literature. For example, Browne & Antonia (1986) and Browne *et al.* (1987) estimated $x_0 \approx -125d$ at $Re_d = 1170$; Aronson & Lofdahl (1993) obtained $x_0 \approx -112d$ at $Re_d = 1840$; Sreenivasan (1981) measured $x_0 \approx -70d$ at $Re_d = 1160$. The present value of x_o differs significantly from that of Aronson & Lofdahl (1993) although the Reynolds numbers are not too dissimilar. This is also observed between Sreenivasan (1981) and Browne & Antonia (1986), Browne *et al.* (1987). This suggests that the initial conditions have a more important effect on x_o than the Reynolds number.

4.3. *A simple means for estimating* $\bar{\epsilon}$

Equation (2.32) provides a simple means for estimating $\bar{\epsilon}$ along the wake axis once $\overline{u^2}$ and R are known. Before checking the accuracy of the present estimates for $\bar{\epsilon}$ with (2.32), the spectral chart method of Djenidi & Antonia (2012) has been applied to the present spectra as an attempt to obtain more accurate values of the energy dissipation rate, when plotted in the form $\phi_u(f)$ versus f. The 'new' estimates of $\bar{\epsilon}$ are denoted by $\bar{\epsilon}_{spec}$. In essence, these values ensure that there is collapse in the upper part of the dissipative range. Since this collapse has a solid analytical underpinning (we recall here that the LI assumption was relaxed in Antonia, Djenidi & Danaila (2014) to an assumption of local axisymmetry), $\bar{\epsilon}_{spec}$ should be very close to the true value of $\bar{\epsilon}$. Figure 9 shows the distribution of $\phi_u^*(k_1^*)$ for several positions over the range $200 < x/d < 600$. The red curves are normalised by $\bar{\epsilon}_{iso}$ and ν, while the blue curves are normalised by $\bar{\epsilon}_{spec}$ and ν. Moreover, for reference, the velocity spectrum on the centreline of a fully developed channel flow is shown (Abe, Antonia & Kawamura 2009). There is a very good agreement between the '$\bar{\epsilon}_{spec}$'-normalised spectra and the channel flow spectrum. On the other hand, the spectra normalised by $\bar{\epsilon}_{iso}$ and ν are shifted up, suggesting that $\bar{\epsilon}_{iso}$ differs from the actual $\bar{\epsilon}$ ($\simeq \bar{\epsilon}_{spec}$). In this case, the ratio

https://doi.org/10.1017/jfm.2015.663 Published online by Cambridge University Press

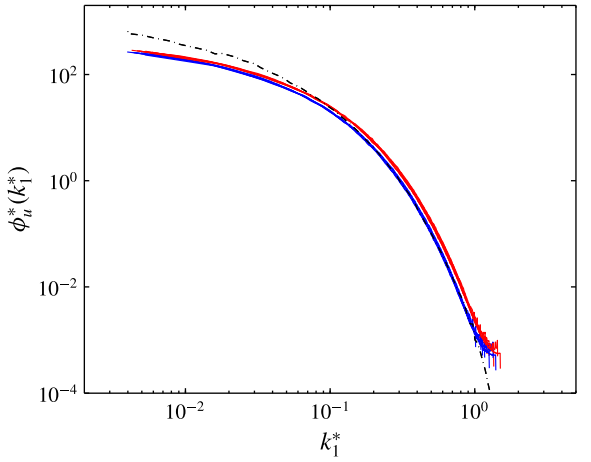

FIGURE 9. (Colour online) Kolmogorov normalised spectra of u over the range $x/d = 200$–600 at $Re_d = 2000$. The red curves are normalised by $\bar{\epsilon}_{iso}$ and ν, while the blue curves are normalised by $\bar{\epsilon}_{spec}$ (the spectral chart method) and ν. The black curve corresponds to the spectrum of u on the centreline of a fully developed channel flow (Abe *et al.* 2009).

$R_\epsilon = \bar{\epsilon}_{iso}/\bar{\epsilon}_{spec}$ is 0.75. We recall that Aronson & Lofdahl (1993) measured the diffusion and advection terms for the one-point kinetic energy budget (2.13), as well as the isotropic dissipation rate $\bar{\epsilon}_{iso}$ in the far wake of a circular cylinder at a comparable Re_d (=1840). Thus, R_ϵ can be estimated as follows:

$$R_\epsilon = \frac{\overline{\epsilon}_{iso}}{\overline{\epsilon}} = \frac{\overline{\epsilon}_{iso}}{\frac{1}{2}U\frac{\partial \overline{q^2}}{\partial x} + \frac{\partial}{\partial y}\left(\frac{1}{2}\overline{u_2 q^2}\right)} = 0.76, \tag{4.3}$$

which is quite close to the value of 0.75 estimated by the spectral chart method at $Re_d = 2000$.

Now, we estimate $\bar{\epsilon}$ with (2.32). At $Re_d = 2000$, Hao *et al.* (2008) showed that both $\overline{u_1^2}/\overline{u_2^2}$ and $\overline{u_1^2}/\overline{u_3^2}$ are approximately 1.4 on the centreline of the far wake. Namely $R = 0.71$ at $Re_d = 2000$. Estimates of $\bar{\epsilon}$ from (2.32) are shown in figure 10 with $A_u = 0.318$, $x_0 = -22d$ and $R = 0.71$ (A_u and x_0 are estimated from the present data). Also shown are the values of $\bar{\epsilon}_{iso}$. The estimated value of R_ϵ from this figure is approximately 0.75 (the square symbols for $\bar{\epsilon}_{iso}/0.75$ collapse reasonably well with $\bar{\epsilon}$), which is in good agreement with the estimate from the spectral chart method above, confirming that (2.32) provides a good and reliable estimate of $\bar{\epsilon}$.

In addition, the predicted value for A_{Re_λ} from (2.38) is 0.92, which is also in agreement with the experimental value of 0.96 at $Re_d = 2000$. Since, as noted in the introduction, there is abundant evidence to indicate that the SP depends on the ICs, the ratios A_{Re_λ}, A_u and c_ϵ should also depend on the ICs. Indeed, as pointed out by Antonia, Zhou & Romano (2002), although the ratio A_{Re_λ} (or $Re_\lambda/Re_d^{1/2}$) is approximately independent of Re_λ at $x/d = 70$ in wakes generated by five different bluff bodies (i.e. a solid circular cylinder, a circular cylinder constructed from a screen of 54 % solidity, a solid square cylinder, a solid plate placed normal to the flow and a screen strip, over a range of Reynolds numbers), its magnitude varies significantly between the wakes at the same Re_d.

https://doi.org/10.1017/jfm.2015.663 Published online by Cambridge University Press

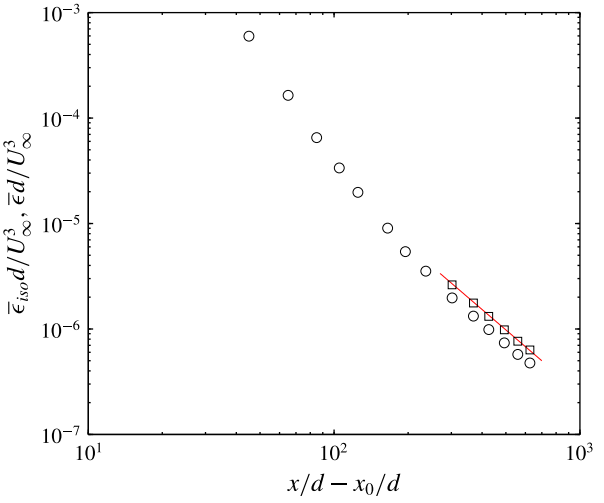

FIGURE 10. (Colour online) Evolution along the centreline of $\bar{\epsilon}$ at $Re_d = 2000$: ○, measured $\bar{\epsilon}_{iso}$; □, measured $\bar{\epsilon}_{iso}/0.75$. The red line is calculated from (2.32) with $A_u = 0.318$, $x_0 = -22d$ and $R = 0.71$.

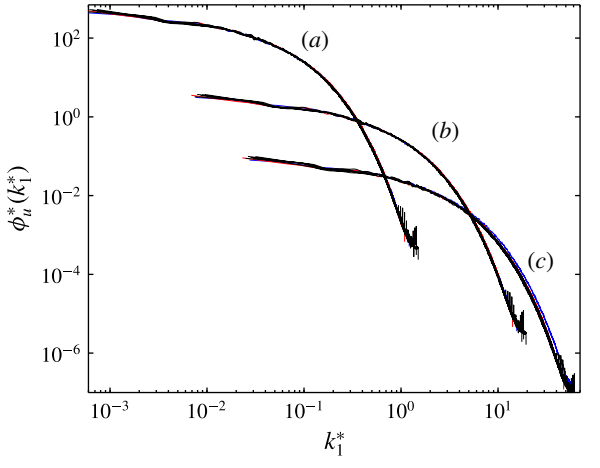

FIGURE 11. (Colour online) Spectra of u over the range $x/d = 200$–600 ($x/d = 211$ (blue), 277, 344, 401, 468, 534 and 601) at $Re_d = 2000$, normalised by (*a*) Kolmogorov scales, (*b*) λ and u', (*c*) U_d and L_0.

5. Test of equilibrium similarity: spectra and structure functions

The single-point flow characterisation of a turbulent wake was described in § 4. In particular, the scaling properties in the far wake were determined and presented. The results can be summarised as follows: the far-wake region of a cylinder can be scaled with any set of length and velocity scales since all scales behave in a similar manner. In this section, we test whether the energy spectra and structure functions comply with SP when normalised by three sets of SP variables: (*a*) Kolmogorov scales; (*b*) λ and u'; (*c*) U_d and L_0. Figure 11 shows the normalised one-dimensional velocity u spectra

https://doi.org/10.1017/jfm.2015.663 Published online by Cambridge University Press

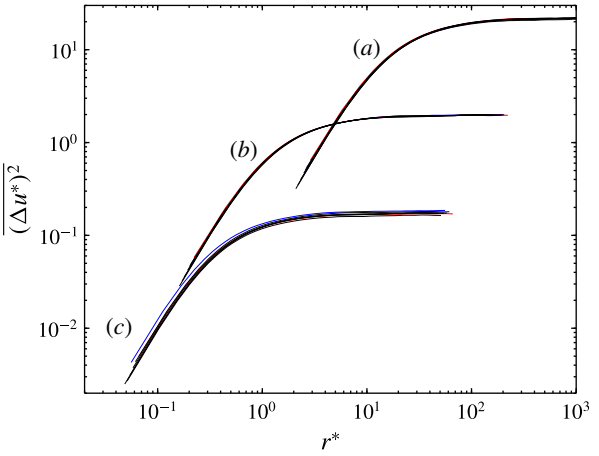

FIGURE 12. (Colour online) Structure functions of u over the range $x/d = 200$–600 ($x/d = 211$ (blue), 277, 344, 401, 468, 534 and 601) at $Re_d = 2000$, normalised by (*a*) Kolmogorov scales, (*b*) λ and u', (*c*) U_d and L_0.

in the range $x/d = 200$–600. There are perfect collapses for the spectra over the entire range of wavenumbers when normalised with the different sets of SP variables for almost all positions in the range $x/d = 200$–600, except for the spectrum normalised with U_d and L_0 at $x/d = 211$. This is related to the local Reynolds number Re_0, which has not reached constancy when $x/d = 211$; it approaches a constant at a slower rate (figure 5) than Re_λ, which is practically constant when $x/d > 200$ (figure 8).

The normalised distributions of the second-order structure function $\overline{(\Delta u^*)^2}$ are plotted in figure 12. The distributions of $\overline{(\Delta u^*)^2}$ present the same level of collapse over the entire range of scales regardless of the set of SP. As expected, because of the reason just mentioned, the distributions normalised with U_d and L_0 at $x/d = 211$ deviate from the others. Of interest, if $\overline{(\Delta u)^2}$ is normalised by the Kolmogorov scales, $\overline{(\Delta u)^2}$ follows (in the dissipative range)

$$\underset{r^*\to 0}{\overline{(\Delta u)^2}} = \frac{r^{*2}}{15}. \tag{5.1}$$

Figure 12 shows that the collapse for $\overline{(\Delta u^*)^2}$ is satisfied in the dissipative range. At the largest values of r^*,

$$\underset{r^*\to \infty}{\overline{(\Delta u^*)^2}} = 2\overline{u^{*2}} = 2(15)^{-1/2} Re_\lambda. \tag{5.2}$$

Since Re_λ is constant over the range $x/d = 200$–600 (see figure 8), $\overline{(\Delta u^*)^2}$ must remain constant, which is indeed supported by figure 12.

If SP is satisfied, one expects that the distributions of the third-order structure function $\overline{(\Delta u)^3}$ should also show a perfect collapse at all scales. This in turn implies that distributions of $(S(r) = \overline{(\Delta u)^3}/\overline{(\Delta u)^2}^{3/2})$, the velocity increment skewness, should also satisfy SP, which is indeed observed in figure 13, showing that the normalised distributions of $S(r)$ collapse relatively well at all separations, irrespective of the set

https://doi.org/10.1017/jfm.2015.663 Published online by Cambridge University Press

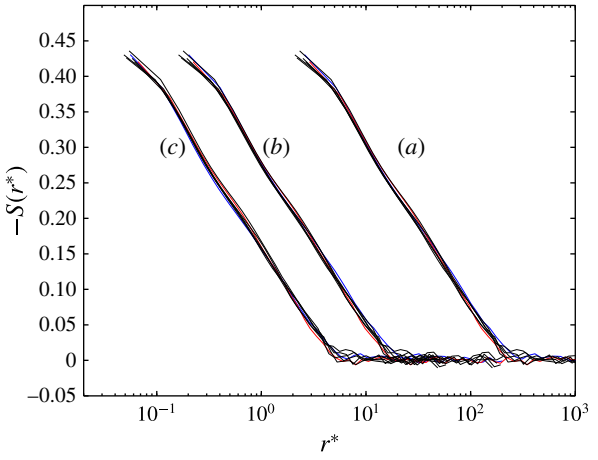

FIGURE 13. (Colour online) Skewness structure functions over the range $x/d = 200$–600 ($x/d = 211$ (blue), 277, 344, 401, 468, 534 and 601) at $Re_d = 2000$, normalised by (*a*) Kolmogorov scales, (*b*) λ and u', (*c*) U_d and L_0.

of SP scaling variables used. Interestingly, the skewness of the longitudinal velocity derivative S is given by

$$S = \lim_{r\to 0} \frac{\overline{(\Delta u)^3}}{\overline{(\Delta u)^2}^{3/2}} = \frac{\overline{(\partial u/\partial x)^3}}{\overline{(\partial u/\partial x)^2}^{3/2}}. \tag{5.3}$$

Thus, figure 13 also indicates that S is constant in the far wake of a cylinder.

In summary, figures 11–13 reveal that SP in the far wake is 'complete', i.e. self-similarity of the energy spectra and the structure functions over the whole range of wavenumbers and scales is satisfied very closely, in accordance with the SP constraint $Re_\lambda =$ constant. Consequently, all turbulent scales vary similarly in the far wake, and any set of length and velocity scales can be used interchangeably for normalisation. The two-point statistics in other flows, e.g. the SP analysis of Burattini *et al.* (2005) and Thiesset *et al.* (2014) in a turbulent round jet, showed that the second- and third-order structure functions and the spectra collapse over a significant range of scales when normalised by λ and $\overline{q^2}$. In grid turbulence, SP at all scales of motion is likely to be achieved only at infinitely large Reynolds number, since Re_λ decreases at finite Reynolds number during the decay, or if the power-law decay exponent n of the turbulent kinetic energy is equal to -1, which is yet to be observed (Djenidi & Antonia 2015). Thus, to the best of our knowledge, the present far wake and the far field of a turbulent round jet are the only flows that satisfy complete SP, i.e. all turbulent scales behave similarly during the decay.

6. Conclusions

Traditional arguments indicate that the mean velocity defect and Reynolds stress profiles in the far wake should exhibit an approximate SP behaviour. However, the influence of the ICs cannot be ruled out, as indicated by George (2012). Many analyses of single-point equations have been reported for the far wake in previous investigations. In this paper, we extend the SP analysis to two-point statistics, i.e. an

https://doi.org/10.1017/jfm.2015.663 Published online by Cambridge University Press

SP analysis of the s.b.s. energy budget equation. Three major conclusions arise from this work.

(i) The power-law variations for the different length scales (namely the integral scale, L_0, the Taylor microscale and the Kolmogorov length scale) and the velocity scales (namely U_d, u' and the Kolmogorov velocity scale) are derived. From the s.b.s. SP analysis, we show that the Reynolds numbers Re_0 and Re_λ, based on the sets (U_d, L_0) and (u', λ) respectively, remain constant in the far wake, indicating that SP is achieved. In particular, the constancy of Re_λ ensures that the ratios between the different length scales and the velocity scales are constant in the far wake. In this case, all of the velocity and length scales can be used interchangeably because they all evolve similarly.

(ii) An exact relation for estimating the evolution of $\bar{\epsilon}$ along the axis is obtained, i.e. (2.32). This equation provides a simple method for estimating $\bar{\epsilon}$ since it requires one only to measure $\overline{u^2}$ and $R = \overline{u_2^2}/\overline{u_1^2}$, and it is supported reasonably well by the hot-wire data in the far wake.

(iii) It is clear that figures 11–13 indicate that the complete SP, i.e. self-similarity of the energy spectra and the structure functions over the whole range of wavenumbers or scales, is satisfied since Re_λ remains constant in the far wake. Thus, the present far wake together with the far field of a turbulent round jet (Burattini *et al.* 2005; Thiesset *et al.* 2014) are the only known flows that satisfy SP completely, i.e. all turbulent scales behave similarly during the decay in these two flows.

Acknowledgement

The financial support by the Australian Research Council is acknowledged.

REFERENCES

ABE, H., ANTONIA, R. A. & KAWAMURA, H. 2009 Correlation between small-scale velocity and scalar fluctuations in a turbulent channel flow. *J. Fluid Mech.* **627**, 1–32.

ANSELMET, F., GAGNE, Y., HOPFINGER, E. J. & ANTONIA, R. A. 1984 Higher-order velocity structure functions in turbulent shear flows. *J. Fluid Mech.* **140**, 63–89.

ANTONIA, R. A. & BROWNE, L. W. 1986 Anisotropy of temperature dissipation in a turbulent wake. *J. Fluid Mech.* **163**, 393–403.

ANTONIA, R. A., BROWNE, L. W. B., BISSET, D. K. & FULACHIER, L. 1987 A description of the organized motion in the turbulent far wake of a cylinder at low Reynolds number. *J. Fluid Mech.* **184**, 423–444.

ANTONIA, R. A., BROWNE, L. W. B. & SHAH, D. A. 1988 Characteristics of vorticity fluctuations in a turbulent wake. *J. Fluid Mech.* **189**, 349–365.

ANTONIA, R. A., DJENIDI, L. & DANAILA, L. 2014 Collapse of the turbulent dissipation range on Kolmogorov scales. *Phys. Fluids* **26**, 045105.

ANTONIA, R. A. & MI, J. 1998 Approach towards self-preservation of turbulent cylinder and screen wakes. *Exp. Therm. Fluid Sci.* **17**, 277–284.

ANTONIA, R. A., ZHOU, T. & ROMANO, G. P. 2002 Small-scale turbulence characteristics of two-dimensional bluff body wakes. *J. Fluid Mech.* **459**, 67–92.

ARONSON, D. & LOFDAHL, L. 1993 The plane wake of a cylinder: measurements and inferences on turbulence modeling. *Phys. Fluids* **5**, 1433–1437.

BATCHELOR, G. K. & TOWNSEND, A. A. 1947 Decay of vorticity in isotropic turbulence. *Proc. R. Soc. Lond.* A **190**, 534–550.

BISSET, D. K., ANTONIA, R. A. & BRITZ, D. 1990*a* Structure of large-scale vorticity in a turbulent far wake. *J. Fluid Mech.* **218**, 463–482.

https://doi.org/10.1017/jfm.2015.663 Published online by Cambridge University Press

BISSET, D. K., ANTONIA, R. A. & BROWNE, L. W. B. 1990*b* Spatial organization of large structures in the turbulent far wake of a cylinder. *J. Fluid Mech.* **218**, 439–461.

BROWN, G. L. & ROSHKO, A. 2012 Turbulent shear layers and wakes. *J. Turbul.* **13**, 1–32.

BROWNE, L. W., ANTONIA, R. A. & SHAH, D. A. 1987 Turbulent energy dissipation in a wake. *J. Fluid Mech.* **179**, 307–326.

BROWNE, L. W. B. & ANTONIA, R. A. 1986 Reynolds shear stress and heat flux measurements in a cylinder wake. *Phys. Fluids* **29**, 709–713.

BURATTINI, P., ANTONIA, R. A. & DANAILA, L. 2005 Similarity in the far field of a turbulent round jet. *Phys. Fluids* **17**, 025101.

CAMUSSI, R. & GUJ, G. 1995 Experimental analysis of scaling laws in low and moderate *Re* grid generated turbulence. *Exp. Fluids* **24**, 63–67.

DANAILA, L., ANSELMET, F., ZHOU, T. & ANTONIA, R. A. 2001 Turbulent energy scale budget equations in a fully developed channel flow. *J. Fluid Mech.* **430**, 87–109.

DJENIDI, L. & ANTONIA, R. A. 2012 A spectral chart method for estimating the mean turbulent kinetic energy dissipation rate. *Exp. Fluids* **53**, 1005–1013.

DJENIDI, L. & ANTONIA, R. A. 2015 A general self-preservation analysis for decaying homogeneous isotropic turbulence. *J. Fluid Mech.* **773**, 345–365.

EWING, D., GEORGE, W. K., ROGERS, M. M. & MOSER, R. D. 2007 Two-point similarity in temporally evolving plane wakes. *J. Fluid Mech.* **577**, 287–307.

GEORGE, W. K. 1989 The self-preservation of the turbulent flows and its relation to initial conditions and coherent structures. In *Advances in Turbulence* (ed. W. K. George & R. Arndt), pp. 39–74. Springer.

GEORGE, W. K. 2012 Asymptotic effect of initial and upstream conditions on turbulence. *Trans. ASME J. Fluids Engng* **134**, 061203.

HAO, Z., ZHOU, T., CHUA, L. P. & YU, S. C. M. 2008 Approximations to energy and temperature dissipation rates in the far field of a cylinder wake. *Exp. Therm. Fluid Sci.* **32**, 791–799.

KOLMOGOROV, A. 1941 Dissipation of energy in the locally isotropic turbulence. *Dokl. Akad. Nauk SSSR* **125**, 15–17.

LEFEUVRE, N., DJENID, L., ANTONIA, R. A. & ZHOU, T. 2014 Turbulent kinetic energy and temperature variance budgets in the far-wake generated by a circular cylinder. In *Proceedings 19th Australasian Fluid Mechanics Conference, Melbourne, Australia*.

MI, J., ZHOU, Y. & NATHAN, G. J. 2004 The effect of Reynolds number on the passive scalar field in the turbulent wake of a circular cylinder. *Flow Turbul. Combust.* **72**, 311–331.

SREENIVASAN, K. R. 1981 Evolution of the centerline probability density function of temperature in a plane turbulent wake. *Phys. Fluids* **24**, 1232–1234.

THIESSET, F., ANTONIA, R. A. & DJENIDI, L. 2014 Consequences of self-preservation on the axis of a turbulent round jet. *J. Fluid Mech.* **748**, R2.

TOWNSEND, A. A. 1951 On the fine-scale structure of turbulence. *Proc. R. Soc. Lond.* A **208**, 534–542.

TOWNSEND, A. A. 1956 *The Structure of Turbulent Shear Flow*, 1st edn. Cambridge University Press.

TOWNSEND, A. A. 1976 *The Structure of Turbulent Shear Flow*, 2nd edn. Cambridge University Press.

WYGNANSKI, I., CHAMPAGNE, F. & MARASLI, B. 1986 On the large-scale structures in two-dimensional, small-deficit, turbulent wakes. *J. Fluid Mech.* **168**, 31–71.

ZHOU, Y. & ANTONIA, R. A. 1995 Memory effects in a turbulent plane wake. *Exp. Fluids* **19**, 112–120.

ZHOU, Y., ANTONIA, R. A. & TSANG, W. K. 1998 The effect of Reynolds number on a turbulent far-wake. *Exp. Fluids* **25**, 118–125.

https://doi.org/10.1017/jfm.2015.663 Published online by Cambridge University Press